

3D Magnetic Patterning in Additive Manufacturing via site-specific in-situ Alloy Modification

Authors

Ariyan Arabi-Hashemi, Xavier Maeder, Renato Figi, Claudia Schreiner, Seth Griffiths,
Christian Leinenbach

Affiliation

Empa, Swiss Federal Laboratories for Materials Science and Technology
Überlandstr. 129, 8600 Dübendorf, Switzerland

Corresponding authors: Christian Leinenbach (Christian.Leinenbach@empa.ch) and Ariyan Arabi-Hashemi (Ariyan.Arab-Hashemi@empa.ch)

Abstract

Controlling the process-microstructure-properties relationship is at the heart of materials science. Thus *in-situ* compositional control in additive manufacturing has the potential to innovate present materials AM processing. We demonstrate *in-situ* alloy modification during laser powder bed fusion (LPBF) processing with the site-specific control of the para- and ferromagnetic properties in a high-nitrogen steel part fabricated by LPBF. Nitrogen can be selectively evaporated during the LPBF process by varying the volumetric energy density. The controlled evaporation of nitrogen stabilizes the ferromagnetic bcc phase at the expense of the paramagnetic fcc phase as shown by experiments and thermodynamic simulations. We demonstrate the feasibility to print complex magnetic structures by a 3D magnetic chessboard pattern comprised of non-ferromagnetic and partially ferromagnetic areas. The presented approach is applicable to all alloys where volatile elements affect the microstructure.

1. Introduction

In recent years, additive manufacturing (AM) of metals (often termed as '3D printing') has evolved from a mere prototyping technology to a real production technology. Laser powder bed fusion (LPBF) or electron beam melting (EBM) has enabled the layer by layer building (Additive) of parts with intricate 3D geometries and new functionalities from metal powders. Different metals such as titanium, nickel, aluminum, cobalt, and iron-based alloys are commercially used to print parts for aerospace, medical, automotive, and machine tool applications[1-4]. The performance of these aforementioned parts is determined by the alloy properties which are governed by the complex interrelationships between the alloy composition, the processing parameters, and the resulting microstructure[3-6]. Furthermore, laser or electron beam-based AM processed parts possess complex thermal histories including rapid solidification of small material volumes, with cooling rates exceeding 10^6 K s^{-1} , followed by multiple heating and cooling cycles with the deposition of subsequent powder layers[7]. During localized melting large thermal gradients (G) and high solidification front velocities (V) result in non-equilibrium elemental partitioning or complete loss of elemental partitioning and meta-stable supersaturated phases[4, 5]. While this may lead to phases with unwanted properties, it also can be exploited for producing parts from materials that are difficult to produce using conventional manufacturing methods such as super-saturated alloys with superior mechanical properties in comparison with conventional alloys[8-10] or oxide dispersion strengthened alloys[11, 12]. The very high energy densities can further lead to compositional variation due to the volatilization of certain elements[5, 13].

Due to directional solidification, microstructures in AM parts are often characterized by columnar grains with (001) texture. It has been shown that microstructure and texture formation during solidification are controlled by the thermal Gradient (G) and the solid-liquid interface velocity (V) and can thus be manipulated to a certain extent by varying the process parameters[14-19]. By carefully manipulating G and V via the process parameters during laser metal deposition and electron beam melting, single crystal laser deposition of Ni superalloys has been achieved[14, 20]. Dehoff et al demonstrated that the grain orientation in a Ni alloy can be varied on a local scale during EBM[15, 21, 22]. This was accomplished by developing electron beam scan strategies based on principles of columnar to equiaxed transitions during solidification. By changing the scan strategy, steady state and/or transient thermal gradients and liquid/solid interface velocity could be promoted, resulting in an equiaxed solidification in certain regions. The microstructure formation in AM fabricated parts can be further manipulated by modifying the composition of the alloys and thereby induce certain phase transformation sequences during solidification[23] or trigger the formation of inoculants that act as nucleation sites[9, 24, 25].

A majority of past research on AM was undertaken to produce equiaxed, crack-free microstructures in order to achieve isotropic mechanical properties of AM fabricated parts. While there is an interest in fabricating metallic components with site-specific mechanical and/or functional material properties, those are still difficult to produce by laser-based AM methods as. The present work demonstrates the feasibility to locally manipulate the para- and ferromagnetic properties of high-nitrogen stainless steel during LPBF by locally controlling the phase and microstructure formation in the material consolidation process.

High-nitrogen stainless steels (HNS) are commercially used due to their high strength and ductility, their excellent corrosion properties, and their biocompatibility in comparison to other stainless steels[26-30]. High amounts of Ni (8-11 wt. %) are usually required to stabilize the fcc-austenite phase in stainless steels. In HNS the austenite phase is stabilized by adding comparably small amounts of N (0.5-1 wt. % N) without any Ni[27]. During the interaction of a laser with an HNS the amount of nitrogen can increase or decrease depending on the nitrogen concentration in the atmosphere[31]. When high-nitrogen steels are welded in a nitrogen-free atmosphere, nitrogen evaporates because of the low nitrogen solubility of the Fe-rich melts[32].

This study demonstrates that the amount of evaporated nitrogen can be controlled locally by varying the energy density, i.e. laser power and scanning speed, during LPBF. The loss of nitrogen results in a loss of fcc phase stability and thus promotes an increase in the amount of ferromagnetic bcc phase present in the microstructure. It is shown that by varying the process parameters, one can locally vary the composition and thus the microstructure of the HNS. This results in a bcc-fcc duplex microstructure with tailored amounts of bcc phase depending on the amount of Nitrogen. Since the bcc phase is ferromagnetic it is possible to build parts with site-specific magnetic properties.

2. Materials and Methods

2.1. Powder

The HNS (1.4452) steel powder had a d_{50} of 45 μm and a size distribution ranging from around 30 μm to 60 μm (Supplement Figure 1 a)). Based on the d_{50} value, the slicing thickness was chosen as 40 μm throughout the study. The powder particles were fully dense and most of the particles were spherical (Supplement Figure 1 b)). The composition of the powder was measured by combustion analysis. All values in wt. %: Cr 16.0, Mn 13.0, Mo 3.3, Si 0.9, C 0.07 and N 0.62.

2.2. Laser powder bed fusion experiments and sample preparation

All LPBF parts were manufactured on a Sisma MySint 100 LPBF machine equipped with a 1070 nm fiber laser, a spot size of 55 μm and a maximum output power of 200 W. The build chamber contained Ar shielding gas at atmospheric pressure. The remaining oxygen in the chamber was around 0.01 % and kept as low as possible to minimize oxidation. The powder layer thickness was set to 40 μm . The volumetric energy density (VED), which is calculated according to

$$VED = \frac{P}{v \cdot h \cdot d} \text{ (Eq. 1)}$$

with P: Laser power, v scan velocity, h: hatch distance, d: powder layer thickness was varied by varying the laser power and the scanning speed. Laser powers used were in the range of 125 W to 200 W and scan velocities ranged between 80 mm/s to 800 mm/s, resulting in VEDs between 31 J/mm³ and 500 J/mm³

Samples were ground using #320 to #4000 grinding paper and polished using 3 μm and 1 μm diamond suspension. Finally samples were polished using 50 nm colloidal silica. To measure melt-pool sizes, samples were etched using V2A etchant (100 ml water, 100 ml HCl, 10 ml HNO₃). The scanning strategy was chosen as simple as possible as meander. It consists of parallel single line laser tracks.

2.3. Density measurements

The density was measured using the Archimedes principle. The weight of the sample was measured in air and in high purity ethanol at room temperature. In order to calculate the density of LPBF parts a full density of 7.77 g/cm³ was used.

2.4. Analysis of nitrogen concentration

The nitrogen concentration was measured by combustion-melting analysis using a LECO TC-500 system. Samples were heated in a graphite double crucible to around 3000°C using an electrode oven. N₂ was measured by a thermal conductivity measuring cell. Certified reference samples and blanks are used for quality assurance. For every measurement two to three independent samples were analyzed. Cylindrical samples required for combustion analysis were directly manufactured by LPBF (Supplementary Figure 4). Weights of the samples were in the range of 250 mg to 500 mg. The error of the measurement was below 0.02 wt. % for all measurements.

2.5. Microstructure characterization

X-ray diffraction was done on a Bruker D8 using Cu K α radiation. A pinhole of 1 mm diameter was used. K β radiation was filtered by a Ni foil. K α 1 was subtracted from all patterns. XRD measurements were done on the same surface as the EBSD measurements. The sample orientation is shown in Figure 3.

The EBSD measurements were done on a Hitachi S4800. The sample was tilted by 70°. The electron beam voltage was set to 20 kV. The step size was 350 nm and only data points with a confidence index >0.05 were considered. Large area EBSD mapping was done in a Tescan Lyra 3 FIB-SEM, using 20 kV and 1.5 μ m step size, with a Digiview V camera from EDAX. Data points with a confidence index >0.01 were considered. All grain sizes provided in the manuscript are based on area fractions.

The lamella for scanning transmission electron microscopy (STEM) analysis was produced from the 500 J/mm³ sample with a FEI Helios NanoLab 600i focused ion beam (FIB). STEM was performed on an FEI Titan Themis microscope equipped with a probe spherical aberration corrector. The microscope was operated at 300 kV and with a 25 mrad probe convergence semiangle. An annular dark field (ADF) detector with a 53 mrad inner / 200 mrad outer collection semiangle was utilized for STEM imaging. The chemical analysis was performed with the SuperEDX (ChemiSTEM technology) system with four silicon drift detectors. Chemical analysis was performed using the Si-K, N-K, Mn-K, Cr-K, C-K, and Fe-K lines.

2.6. Vibrating sample magnetometry

Vibrating sample magnetometry (VSM) was done on a physical property measurement system by Quantum Design. All measurements were done at 27°C. Samples with a typical weight in the range of 50 mg-100 mg (volume \sim mm³) were cut out of LPBF build parts by a rotating saw.

2.7. Thermodynamic simulations

Thermodynamic calculations were performed using ThermoCalc version 2019 in combination with the database TCFE7. Beside the calculation of vertical sections for the given alloy composition and amounts of N between 0 and 1 wt.%, the phase fractions of the fcc and bcc phases upon solidification were calculated for different amounts of N between 0.3 and 0.8 wt.% using the Scheil-Gulliver model. The calculations were performed for a pressure $p = 10^5$ Pa.

In addition, T_0 temperatures were calculated for the phase transformations liquid \rightarrow bcc and liquid \rightarrow fcc using the same database. The so called T_0 temperature is the temperature at which the Gibbs free energies of two phases, G_A and G_B , are equal with the same composition. Under equilibrium conditions, the energy is minimized by the formation of two phases with a different composition. However, at rapid cooling conditions diffusion is strongly reduced, which can hinder the formation of the equilibrium phases. The formation of the low temperature phase A is expected as soon as $T < T_{0,A\rightarrow B}$, where $G_A < G_B$. Consequently, the formed phases are metastable as the energy of the intersection point of the Gibbs free energy curves where $G_A = G_B$ is always larger than the energy of the points lying on the common tangent line.

3. Results and Discussion

3.1. Phase and microstructure formation during LPBF

Microstructure in as-printed parts

Conduction mode welding was observed in all of the conditions tested. Optical micrographs of representative microstructures and melt pools are shown in Figure 1. Material densities of as-built parts were measured by the Archimedes' principle. For a VED $< 50 \text{ J/mm}^3$ parts were not dense due to insufficient melting of the powder. For a VED $> 50 \text{ J/mm}^3$ parts with a density $> 99.5 \%$ were achieved. A VED of 54 J/mm^3 was sufficient to create a dense part with an underlying melt pool depth of $\sim 50 \mu\text{m}$ and a melt pool width of $\sim 200 \mu\text{m}$ (Figure 1 c)). For the highest VED of 500 J/mm^3 the melt pool size increased to a depth of $\sim 200 \mu\text{m}$ and a width of $\sim 350 \mu\text{m}$. For this VED each melt layer is remolten for ~ 5 times since the layer thickness was constantly $40 \mu\text{m}$ throughout the study.

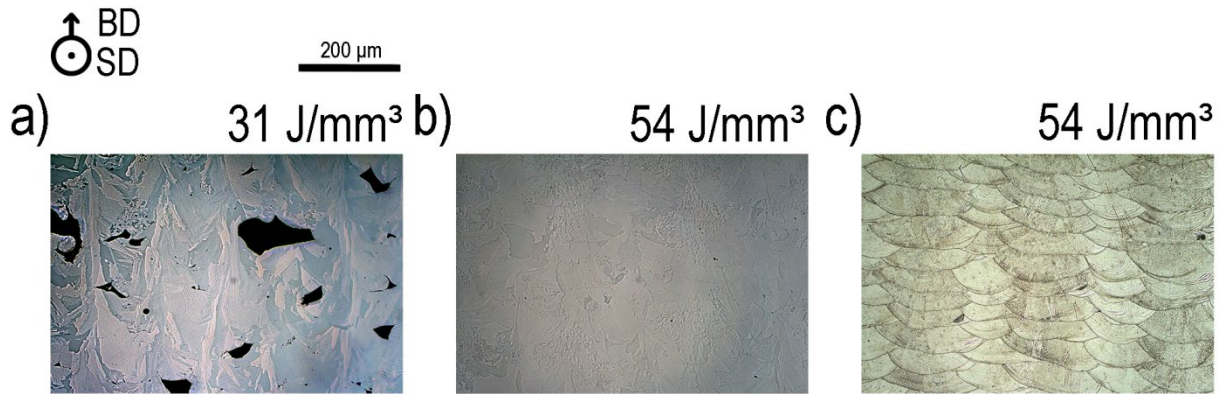


Figure 1: Optical micrographs showing a) insufficient powder melting b) a dense as-built part c) the melt pool geometry revealed by V2A etching. The build direction (BD) and laser scanning direction (SD) are shown.

In order to reveal the phases present in LPBF parts, x-ray diffraction patterns were taken from samples produced with a VED of 50 J/mm^3 (lowest VED required for full density) and the highest VED of 500 J/mm^3 (Figure 2). The diffraction pattern shows that the main phases in the build parts are fcc-austenite and bcc-ferrite. While for a VED of 50 J/mm^3 the part is fully austenitic, a VED increase to 500 J/mm^3 leads to a pronounced increase of the amount of the bcc phase. Based on the peak intensities of the fcc (111) to bcc (110) peaks, the phase fraction of bcc is 55 % while the phase fraction of fcc is 45 %. These values should be taken as first approximations because texture is present in the samples which affect the result. Texture can be inferred by the almost absence of the bcc (200) peak for the 500 J/mm^3 sample and also from the low intensity of the fcc (200) peak for the 50 J/mm^3 . In a texture-free sample this peak should account for about 50 % of the intensity of the (111) peak.

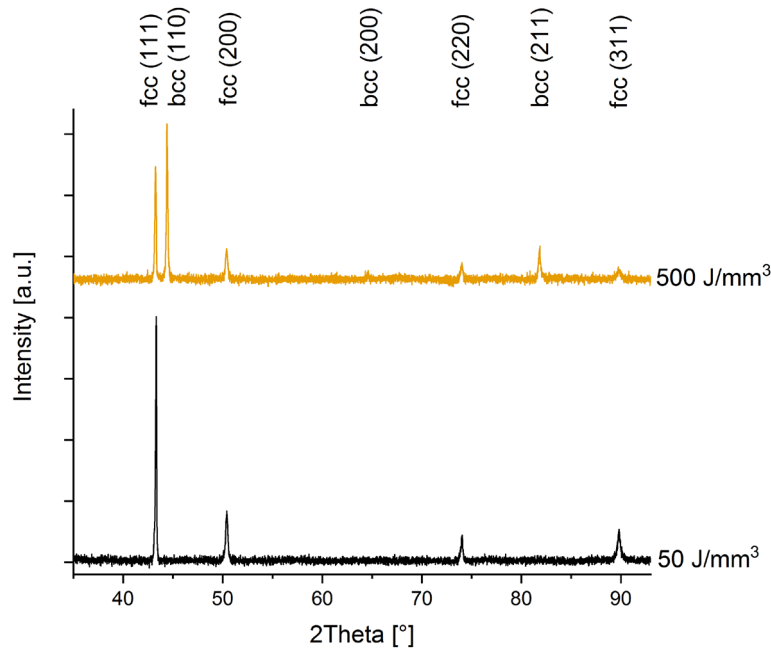


Figure 2: X-ray diffraction patterns for two different VEDs. While the 50 J/mm³ sample is fully austenitic, a VED of 500 J/mm³ creates the ferritic phase at the expense of the fcc phase.

EBSD measurements elucidate the microstructural evolution as a function of the VED (Figure 3). Samples produced at three VEDs were selected: 50 J/mm³ (low VED), 160 J/mm³ (intermediate VED) and 500 J/mm³ (high VED). Considering the XRD results a phase composition consisting of fcc and bcc was assumed for the EBSD measurements. For a VED of 50 J/mm³ a comparably large grained microstructure is observed with an average grain size of 55 μm . A crystallographic analysis shows that the long axis of the columns is parallel to the [001] direction. Each large grain consists of many small subgrains connected by small-angle grain boundaries. The formation of these subgrains is typical for the LPBF process[33]. For an intermediate VED of 160 J/mm³ the amount of fcc phase decreased to 94 % and an average grain size of 9 μm is observed. Again the growth direction of the fcc grains is along the [001] direction. Between the fcc grains, bcc grains in the size range of 2 μm diameter are found. In comparison to the intermediate VED the grain size for 500 J/mm³ increased to 15 μm . For the VED of 500 J/mm³ the microstructure contains 42 vol. % bcc and 58 vol. % fcc.

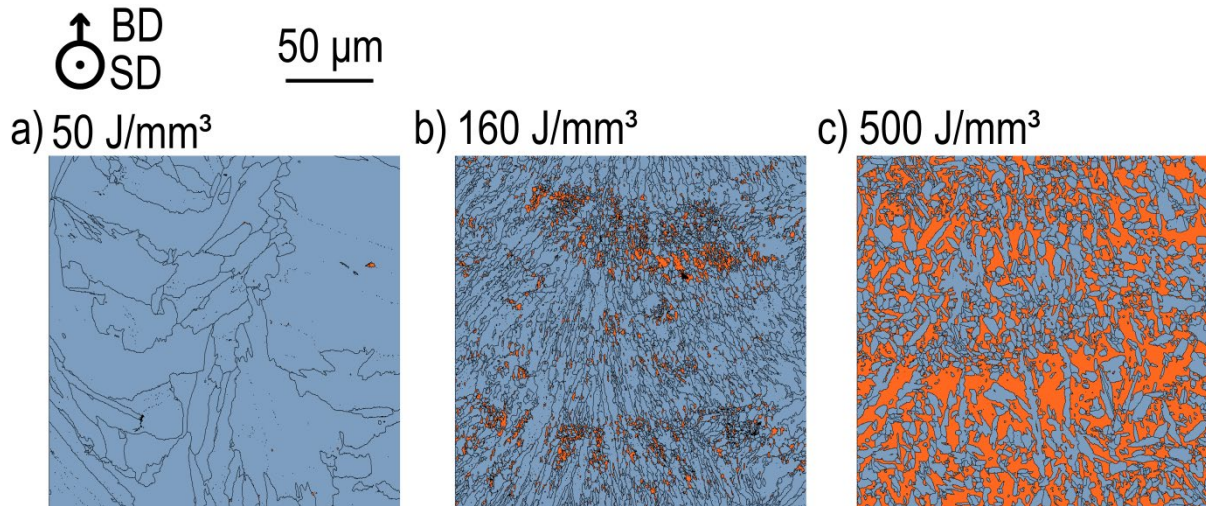


Figure 3: EBSD phase maps showing the microstructural evolution for increasing VEDs. Blue: austenite fcc and orange: ferrite bcc. a) For 50 J/mm³ large austenitic grains are observed. b) For 160 J/mm³ fcc grains and bcc grains are present. The bcc phase fraction is 6 %. c) For 500 J/mm³ fcc and bcc grains are present. The bcc phase fraction grew to 42 %.

The nitrogen concentration was measured for the powder and also for LPBF samples with different VEDs (Figure 4 a)). The powder showed an initial concentration of 0.62 wt. % N. For a small VED of 31 J/mm³ (insufficient melting) the concentration of N stayed identical to the concentration of N in the powder. A VED of 500 J/mm³ resulted in a concentration of 0.34 wt. % N. A STEM/EDX measurement was done on fcc and bcc grains of the sample with the highest VED of 500 J/mm³ (Figure 4 b)). Segregation of N, Si and Mn was observed between the fcc and bcc phases. The individual phases of the grains were identified by the analysis of the fast fourier transformations (FFT) of high-resolution ADF-STEM images which are shown in Supplement Figure 3. Figure 4 b) shows clearly that the fcc phase is N and Mn enriched while the bcc phase is Si enriched. All the other alloying elements (Fe, C, Cr and Mo) were homogeneously distributed (Supplementary Figure 3).

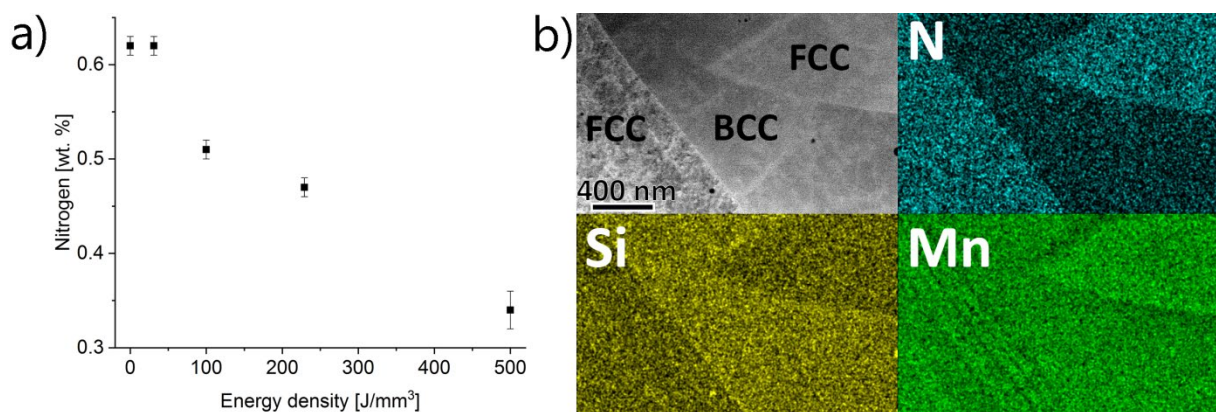


Figure 4: a) The nitrogen concentration decreases for increasing VEDs. While the powder (0 J/mm³) shows a N concentration of 0.62 wt. %, a VED of 500 J/mm³ results in a N concentration of 0.34 wt. %. b) STEM-EDX maps showing segregation of N, Si and Mn for a VED of 500 J/mm³. No significant segregation of Fe, C, Cr and Mo was observed. While the fcc phase is enriched with N and Mn, the bcc phase is enriched with Si.

Nitrogen evaporation upon melting

Nitrogen influences the fcc and bcc phase formation and stability which is calculated in the pseudo-binary phase diagrams (varying only N concentration) shown in Figure 5.

Figure 5 a) shows the calculated phase diagram that considers the gas phase, mainly consisting of N₂. For the nitrogen concentration of the as-delivered powder of 0.62 wt. %, this gas phase is stable for temperatures above approximately 1300°C. Temperatures of the melt in laser processing can exceed 2000°C⁷. Due to the absence of N₂ in the atmosphere, overall the nitrogen evaporates at temperatures above 1300°C. It can be seen that with increasing temperature the liquid phase has a decreasing solubility for N which means that the driving force for N to evaporate increases.

Dong et al. observed that the extent of N evaporation during laser welding of a HNS is dependent on the temperature and the N₂ partial pressure in the surrounding atmosphere[32]. Since Ar is constantly streaming during the process, evaporated N and other alloying elements are rapidly carried away from the melt pool.

In the present case, it is assumed that the extent of nitrogen loss is approximately proportional to the melt pool life time and the ratio of the exposed area of liquid metal to the volume of the melt pool. The melt pool life time and the ratio of the area of liquid metal to the volume of the melt pool can be estimated by using the Rosenthal equation[34].

$$T = T_0 + \frac{Q}{2\pi\kappa r} \exp\left(-\frac{v(r+\xi)}{2\alpha}\right) \quad (\text{Eq. 2})$$

With $\alpha = \frac{\kappa}{\rho C}$ and $r = (\xi^2 + y^2 + z^2)$ the radial distance from the weld beam in a reference frame traveling with the laser beam. Q is the absorbed power, κ the thermal conductivity, T_0 the substrate temperature, v the laser speed, ρ the material density C the heat capacity

The length L and the width W of the melt pool can be approximated by

$$L \approx \frac{Q}{2\pi\kappa(T_m - T_0)} \quad (\text{Eq. 3})$$

and

$$W \approx \sqrt{\frac{8Q}{e\pi C v(T_m - T_0)}} \quad (\text{Eq. 4})$$

with T_m the melting temperature[35, 36]. The melt pool lifetime L/v is thus proportional to Q/v . The ratio of melt pool area to the total volume of the melt pool scales with $1/W$ which is proportional to $\sqrt{v/Q}$. The amount of evaporated nitrogen is then proportional to $\sqrt{Q/v}$. The VED is given by Eq. 1 Since the hatch spacing and the layer thickness were kept constant in the present study and assuming that the absorbed power is proportional to the laser power, the amount of lost nitrogen is proportional to \sqrt{VED} . This simple model neglects the temperature-dependant solubility of N of the material. The solubility of N in the melt decreases with increasing temperatures above 1300°C. Therefore, the driving force for N to evaporate increases for increasing maximum melt pool temperatures caused by an increased laser power or a decreased laser velocity. Nevertheless, the suggested loss of N which should be proportional to \sqrt{VED} agrees reasonably well with the experimental data shown in Figure 4 a) where the largest loss of N is observed for small VEDs.

Rapid solidification and phase selection

Figure 5 b) shows the same vertical section as shown in Figure 5 a), but calculated without considering the gas phase. Under near-equilibrium conditions for N concentrations <0.8 wt. %, the phase diagram suggests that the primary phase upon solidification is bcc (Figure 5 b)). The amount of bcc should significantly increase with decreasing amounts of N. However, this is not confirmed by our observations on samples with nitrogen concentration of ~0.5 wt. %, where almost only fcc and very little bcc were detected. The Scheil model does not predict the fcc/bcc phase fractions correctly for N concentrations above 0.5 wt. %. For a concentration of 0.5 wt. % N a bcc phase fraction of 50 % is predicted using the Scheil-Gulliver model, whereas less than 5 % are observed experimentally.

Phase selection between bcc and fcc in Fe-Cr-Ni steels during solidification is a well-known phenomenon and has been studied by various authors in the past[37-40]. A phase transition from stable bcc to metastable fcc has been observed with increasing solidification front velocity. The critical transition velocity has been found to be dependent on the ratio between bcc stabilizing elements (e.g. Cr) and fcc stabilizing elements (e.g. Ni, C, N) Cr_{eq}/Ni_{eq} and on the thermal gradient. A transition from fcc to bcc is obtained when the amount of fcc stabilizers is reduced or when the solidification front velocity is slowed down[38]. Assuming that the nucleation for the two competing phases bcc and fcc is abundant, the phase with the highest interface temperature is considered to be the kinetically most stable one. The maximum interface temperature for all competing phases can be obtained by calculating the corresponding interface response functions. For steels with a Cr_{eq}/Ni_{eq} between 1.5 and 1.8 that are subjected to thermal gradients of $G = 15 \text{ K mm}^{-1}$ as they occur e.g. during welding (i.e. in comparably large melt pools), critical solidification front velocities between approximately 0.001 and 10 mm s^{-1} are reported[38, 39].

For powder bed fusion of stainless steel 316L at parameters comparable to the ones applied in this work, cooling rates \dot{T} on the order of $2\text{-}5 \times 10^6 \text{ K s}^{-1}$ and thermal gradients between $G = 1 \times 10^4$ and $1 \times 10^5 \text{ K mm}^{-1}$ have been reported[41]. The corresponding solidification front velocities in a single melt pool can be estimated according to

$$V = \frac{\dot{T}}{G} \text{ (Eq. 5)}$$

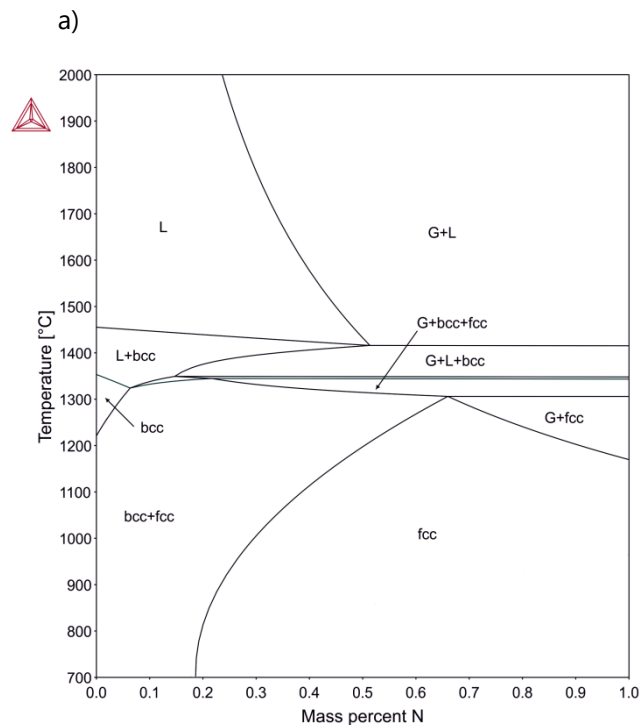
Assuming that the thermo-physical properties of the HNS studied in this work and 316L are similar, the values for V thus range between 20 and 500 mm s^{-1} in the present case, which is significantly higher than the ones mentioned above. Such high solidification front velocities lead to highly non-equilibrium conditions with strongly reduced diffusion that can result in (near-)partitionless solidification. It has been shown in previous work that the phase transformations under such conditions can be predicted considering phase selection hierarchy maps based on calculated T_0 temperatures [42]. Comparing the equilibrium phase diagram with the T_0 calculations explains and predicts the extension of phase fields and changed transformation behavior under rapid solidification and cooling conditions. Considering the high cooling rates and short melt pool lifetimes, it can be assumed that the gas phase does not need to be considered during rapid solidification.

In Figure 5 b) the calculated T_0 temperatures for the transitions liquid→fcc and liquid→bcc are shown as dotted lines. These lines intersect at a N concentration of around 0.38 wt. \% . When considering higher N concentrations, i.e. in samples produced at low VEDs, the fcc phase is likely to form first while at lower N concentrations, bcc is the preferred primary phase that forms from the melt. We thus conclude that

for small VEDs and small melt pools the T_0 concept can be applied which explains the experimentally observed fcc phase in the range of 0.51 – 0.62 wt. % N. At the same time the T_0 concept predicts the formation of the bcc phase for concentrations below 0.38 wt. % which is in agreement with the experimental findings where an increase of bcc is observed below a N concentration of 0.47 wt. %.

Samples produced at higher VEDs show larger melt pools and a more pronounced loss of N (Figure 4 a)). The melt pool lifetimes are longer and the solidification front velocities reach comparably low values (V can be further decreased due to the accumulated heat in the part) so that (near-) partitionless solidification no longer occurs as shown by the segregation of N, Si and Mn obtained for a VED of 500 J/mm³ (Figure 4 b)). For a N concentration of 0.3 wt. % a bcc phase fraction of 75 % is calculated using the Scheil-Gulliver model, while experimentally 42 % are observed. Despite this difference between the calculated and measured phase fractions, these results indicate that the deviation from equilibrium conditions is less pronounced for larger melt pools and that a phase selection based on the T_0 concept is no longer applicable for N concentrations below 0.47 wt. % (high VEDs). In this case, bcc becomes the primary phase, and the amount of bcc increases with decreasing amount of N.

The situation during LPBF of the HNS is rather complex in comparison to welding due to the multiple re-heating and cooling. In addition, changes of the solidification conditions correlate with changes of the amount of N. However, due to the large influence of small changes of N on the phase stability of the present alloy as discussed in the previous section it is assumed that changes in the alloy composition are the main driving force for the phase formation of the present alloy.



b)

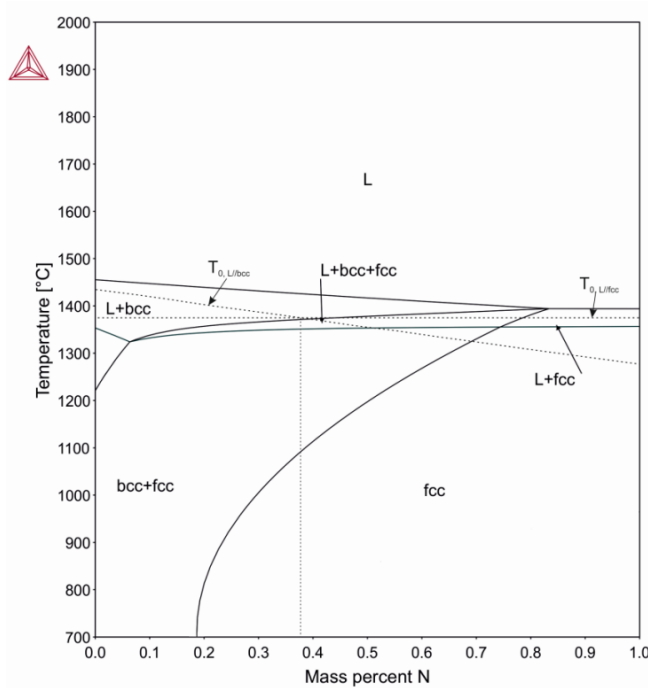


Figure 5: Phase diagram as a function of the nitrogen concentration a) with gas phase (mainly N₂) included, b) without considering the gas phase. The T_0 temperatures for the transitions liquid→fcc and liquid→bcc are shown by dotted lines. The curves intersect at 0.38 wt. % N.

3.2. Characterization of magnetic properties and 3D magnetic patterning

The bulk samples produced with different VEDs were magnetically characterized using VSM (cf. Figure 6 a)). As observed by XRD two phases are present: fcc austenite and bcc ferrite. In order to obtain the saturation magnetizations, the linear paramagnetic response was subtracted for each magnetization measurement. The bcc phase is the only ferromagnetic phase present. Therefore the saturation magnetization of LPBF parts is linearly proportional to the bcc phase fraction. The saturation magnetization can be used to quantify the bcc phase fraction in the LPBF samples. Phase quantification by VSM has the advantage over the phase quantification by EBSD since VSM probes a representative bulk volume instead of a small surface during EBSD measurements. In order to do phase quantification using the saturation magnetization of the individual samples, the saturation magnetization of the bcc phase must be known. This value was calculated by combining EBSD and VSM results for the 500 J/mm³ sample. For this VED, EBSD showed a phase fraction of bcc of 42 %, while VSM showed that this amount of bcc phase corresponds to a saturation magnetization of 40 emu/g. The saturation magnetization of a fully ferritic bcc material is thus 95 emu/g. The bcc phase fraction was calculated based on the saturation magnetization obtained for different VEDs using the obtained saturation magnetization of 95 emu/g for a fully ferritic material (Figure 6 b). Three different regions can be distinguished based on the amount of bcc phase ranging from ~2 to 4 vol.%, ~5 to 8 vol.%, and 21 to 42 vol.%. These three different regions can be assigned to the three different microstructures presented in the EBSD maps in Figure 3: i) Large fcc grains with ~2 to 4 vol.% bcc, ii) small sized grains with ~5 to 8 vol.% bcc and iii) intermediate sized grains with 21 - 42 vol.% bcc.

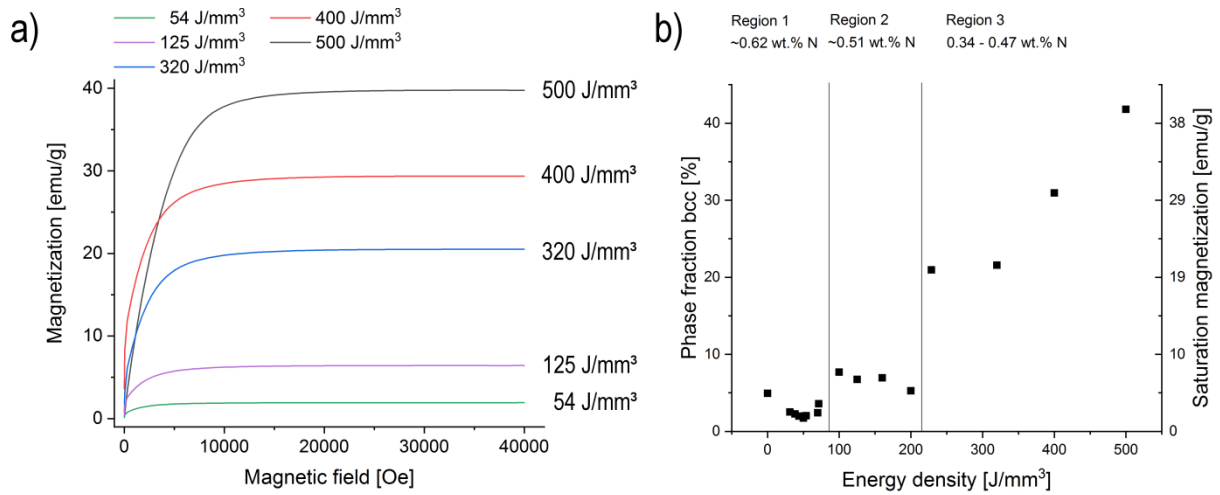


Figure 6: a) Magnetization curves $M(H)$ showing the saturation magnetization as a function of the energy input. b) Based on the saturation magnetization the bcc phase fraction was calculated. Three different phase regions are identified. The phase fraction and the saturation magnetization of the powder are shown at 0 J/mm^3 . The N concentrations for the three regions are shown.

As shown in Figure 6 b) the phase fraction of the bcc phase can be controlled by varying the VEDs during LPBF. For VEDs between 50 J/mm^3 to 500 J/mm^3 dense parts were obtained with varying bcc phase fractions ranging between 2 vol.% and 42 vol.%, respectively. This allows to locally control the ferromagnetic properties of LPBF parts. In order to reveal the high potential of processing HNS by LPBF to create complex 3D magnetic structures a cuboid demonstrator was printed with dimensions of $4 \text{ mm} \times 4 \text{ mm} \times 3 \text{ mm}$ (Figure 7 a) and b)). The cuboid was manufactured using two different VEDs of 54 J/mm^3 and 229 J/mm^3 . While 54 J/mm^3 gives an almost fully austenitic structure, processing with 229 J/mm^3 will locally create 21 % bcc phase. The cuboid consists of 16 small cuboids with dimensions of $1 \text{ mm} \times 1 \text{ mm} \times 3 \text{ mm}$ (length x width x height). Figure 7 a) shows the individual laser scanning tracks with a hatching distance of $125 \mu\text{m}$. Each field consists of 8 scanning tracks giving a field width of $8 \times 125 \mu\text{m} = 1 \text{ mm}$. For the grey regions a low VED of 54 J/mm^3 was used while for the green regions a VED of 229 J/mm^3 was used. The alternating use of low and high VEDs creates a chessboard pattern with alternating magnetic properties. After LPBF the top surface was ground. An optical micrograph is shown in Figure 7 c). From this micrograph no information about the magnetic properties can be obtained. In order to reveal the magnetic structure, a ferromagnetic powder was dispersed over the ground surface of the cuboid and a permamagnet was put close to the cuboid. As a consequence, the magnetic particles from areas where the bcc phase was absent were attracted by the permamagnet due to weak magnetic bonding of the powder particles to the surface. The particles remained on the surface at areas of magnetic attraction due to the presence of the bcc phase (Figure 7 d)).

An optical micrograph of a polished surface shows the different regions processed with low and high VEDs (Figure 7 e)). The areas are not equivalently sized as planned in the CAD input file where each square should have dimensions of $1 \text{ mm} \times 1 \text{ mm}$. Instead, the areas created by the higher VED of 229 J/mm^3 are larger compared to the areas created by the lower VED of 54 J/mm^3 . Therefore the desired dimensions of equally large magnetic and non-magnetic domains were not achieved. The increased size of the magnetic areas is attributed to the larger melt pool dimensions underlying the higher VED. By

properly considering the melt pool dimensions a precise control of the size of magnetic and non-magnetic areas should be achievable.

An EBSD phase map of four areas is shown in Figure 7 f). These four areas are marked by a green rectangle in Figure 7 d). The cuboids printed with 54 J/mm^3 are indeed fully austenitic as expected, i.e. Figure 7 e) marked in green. The regions printed with 229 J/mm^3 reveal an inhomogeneous distribution of the bcc phase. Gradients of the bcc phase distribution within each of two bcc containing $1 \text{ mm} \times 1 \text{ mm}$ squares are visible: From top to bottom the amount of bcc phase is increasing. Additionally at the horizontal borders of the different areas straight lines with almost 100 % bcc phase fraction are observed.

The spatial resolution of phase patterning due to N evaporation is directly linked to the melt pool size. As mentioned above melt pool sizes (depth x width) ranged between $50 \text{ }\mu\text{m} \times 200 \text{ }\mu\text{m}$ and $200 \text{ }\mu\text{m} \times 350 \text{ }\mu\text{m}$ for a VED of 54 J/mm^3 and 500 J/mm^3 , respectively. The Nitrogen content of the alloy can locally be reduced by increasing the laser power and decreasing the speed which increased the width of the melt pool. The increase of the width of the melt pool is detrimental to achieve a high patterning resolution. Multiple rescanning with low energy densities of the same area might be a way to evaporate sufficient N while maintaining a high spatial resolution of the patterning process due to small melt pool sizes.

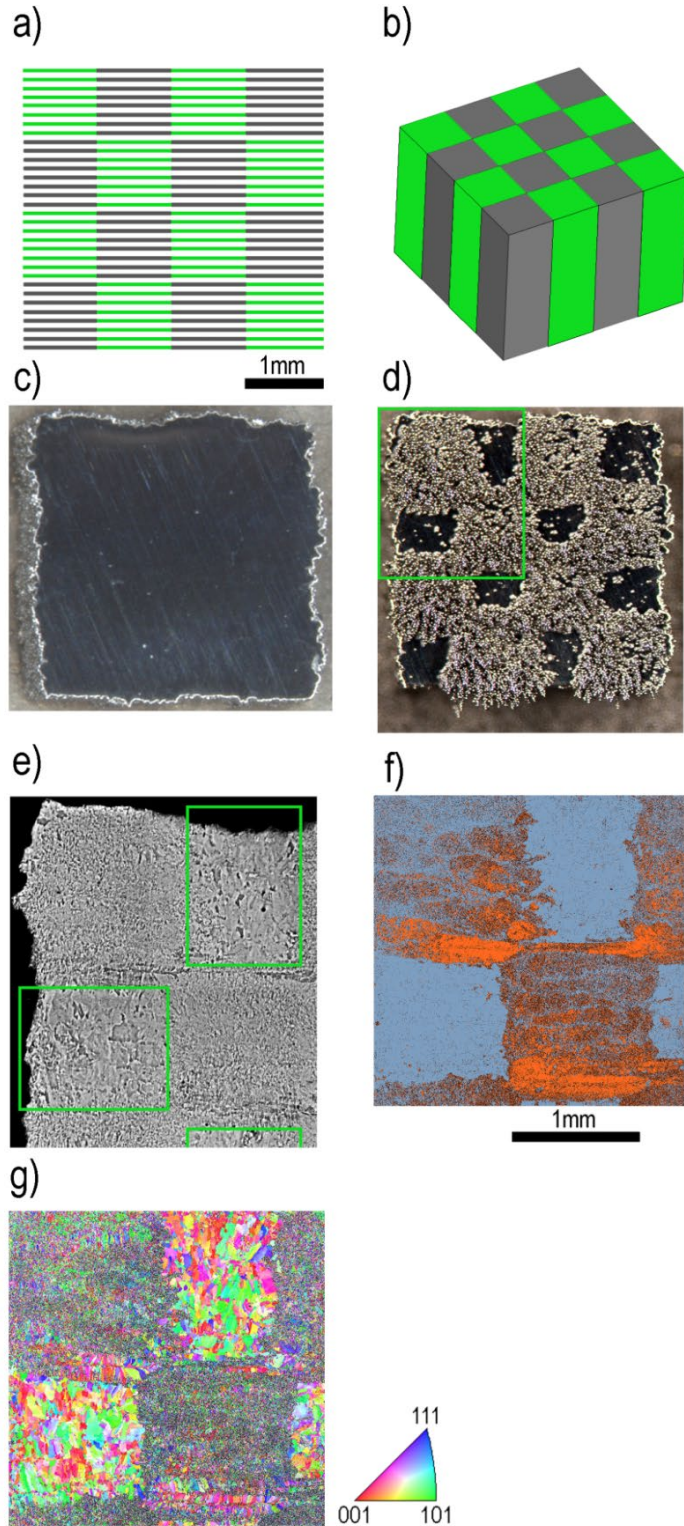


Figure 7: For all images shown the building direction is pointing towards the reader. a) Applied scanning strategy showing the individual laser scan tracks with a hatching distance of 125 μm . Two different VEDs were used: Green 229 J/mm³ and black 54 J/mm³. b) 3d image of the cuboid c) The ground surface indicates a dense part. d) Magnetic spheres reveal the magnetic chessboard pattern. The green box indicates the area of the measurement shown in e) to g). e) Optical micrograph showing differences in the microstructures for the different VEDs. f) EBSD phase map (blue: fcc and orange: bcc) revealing the phase composition of four different fields. g) EBSD inverse pole figure map shows larger grains in the fully austenitic regions and a fine grained microstructure for the bcc and fcc containing areas.

4. Conclusion

This work demonstrates the feasibility of manipulating the para- and ferromagnetic properties on a local scale of a high-nitrogen stainless steel during LPBF by site-specific *in-situ* alloying. In the present case the controlled evaporation of the fcc-stabilizing element N was achieved by local variations of the melt pool geometry, which is a function of the VED. Samples produced at low VEDs showed almost no bcc phase which is explained by a kinetic preference to form fcc at high solidification front velocities. The amount of bcc phase increased with increasing VED. An increase of the VED causes longer lifetimes of the melt pool alongside higher maximum temperatures of the liquid phase. Assuming nitrogen is mainly lost during the melting step, both the increase of the maximum temperature and the increase of the melt pool lifetime favors the loss of nitrogen. In addition to an increase of temperature and melt-pool lifetime, the melt-pool size, i.e. depth and area, increased for increasing energy densities. A multiple remelting of layers (each layer up to 5 times for 500 J/mm³) and an increase of the melt pool area in contact with the gaseous Ar phase favors the loss of nitrogen. Besides a loss of the austenite stabilizing element N, a segregation of N between the fcc and bcc phases was observed (Figure 4 b)). Varying the VEDs allows fabricating parts with spatially varying magnetic properties. A 3D magnetic chessboard was printed to reveal the potential of the process of in-situ alloy modification.

The generally undesired evaporation of elements, in this case N, is deliberately used to control the phase composition between fcc and bcc over a wider range. The approach to locally control the fraction of a volatile element can also be used for other alloys as for example NiTi shape memory alloys. For NiTi a small change of composition in the range of 0.1 at. % has a severe impact on the phase transformation temperatures. The volatile element Ti could be locally evaporated to change the local phase transformation temperature. Following this approach NiTi shape memory alloys with unique thermo-mechanical properties could be fabricated. The presented approach is also applicable for all alloy compositions close to phase boundaries where slight changes of volatile elements have a severe impact on the local phase content. By gradually changing the power or scanning speed of the laser along a scan line, graded materials with locally continuous microstructural transitions could be manufactured. LPBF is a unique process to manufacture materials with locally varying properties. The presented approach can be used for other materials containing volatile elements.

Acknowledgment

Parts of the work were financed by the Swiss Innovation Agency (project Nr. 27554.1 PFIW-IW). The authors thank the company Hempel Special Metals AG, Dübendorf, Switzerland, for providing the HNS powder. K. Zweiacker is acknowledged for proofreading the manuscript. The authors further thank H. J. Hug and A.-O. Mandru for their help with the magnetic measurements, and M. Rossell for help with STEM analysis.

Author contributions

AAH printed all LPBF build parts, did the powder characterization and the XRD, EBSD and VSM measurements. CL performed the Calphad simulations. XM performed the large scale EBSD measurement. SG did the FIB lamella preparation and STEM measurements. RF and CS analysed the Nitrogen content of the powder and the LPBF cylinders. AAH and CL wrote the manuscript. All the authors contributed to and read the final manuscript.

References

1. Babu, S.S., et al., *Additive manufacturing of materials: Opportunities and challenges*. MRS Bulletin, 2015. **40**(12): p. 1154-1161.
2. Herzog, D., et al., *Additive manufacturing of metals*. Acta Materialia, 2016. **117**: p. 371-392.
3. DebRoy, T., et al., *Additive manufacturing of metallic components – Process, structure and properties*. Progress in Materials Science, 2018. **92**: p. 112-224.
4. Sames, W.J., et al., *The metallurgy and processing science of metal additive manufacturing*. International Materials Reviews, 2016. **61**(5): p. 315-360.
5. Collins, P.C., et al., *Microstructural Control of Additively Manufactured Metallic Materials*. Annual Review of Materials Research, 2016. **46**(1): p. 63-91.
6. Wang, Y.M., et al., *Additively manufactured hierarchical stainless steels with high strength and ductility*. Nat Mater, 2018. **17**(1): p. 63-71.
7. Hooper, P.A., *Melt pool temperature and cooling rates in laser powder bed fusion*. Additive Manufacturing, 2018. **22**: p. 548-559.
8. Schmidtke, K., et al., *Process and Mechanical Properties: Applicability of a Scandium modified Al-alloy for Laser Additive Manufacturing*. Physics Procedia, 2011. **12**: p. 369-374.
9. Spierings, A.B., et al., *Microstructural features of Sc- and Zr-modified Al-Mg alloys processed by selective laser melting*. Materials & Design, 2017. **115**: p. 52-63.
10. Spierings, A.B., et al., *Microstructure and mechanical properties of as-processed scandium-modified aluminium using selective laser melting*. CIRP Annals, 2016. **65**(1): p. 213-216.
11. Kenel, C., et al., *Microstructure and oxide particle stability in a novel ODS γ -TiAl alloy processed by spark plasma sintering and laser additive manufacturing*. Intermetallics, 2017. **90**: p. 63-73.
12. Kenel, C., et al., *Selective laser melting of an oxide dispersion strengthened (ODS) γ -TiAl alloy towards production of complex structures*. Materials & Design, 2017. **134**: p. 81-90.
13. Semiatin, S.L., V.G. Ivanchenko, and O.M. Ivasishin, *Diffusion models for evaporation losses during electron-beam melting of alpha/beta-titanium alloys*. Metallurgical and Materials Transactions B, 2004. **35**(2): p. 235-245.
14. Gäumann, M., et al., *Single-crystal laser deposition of superalloys: processing-microstructure maps*. Acta Materialia, 2001. **49**(6): p. 1051-1062.
15. Dehoff, R.R., et al., *Site specific control of crystallographic grain orientation through electron beam additive manufacturing*. Materials Science and Technology, 2014. **31**(8): p. 931-938.
16. Saadi, S., *An Investigation into Microstructure and Microstructural Control of Additive Layer Manufactured Ti-6Al-4V by Electron Beam Melting*. PhD theses, 2011: p. 238.
17. Narra, S.P., et al., *Location specific solidification microstructure control in electron beam melting of Ti-6Al-4V*. Additive Manufacturing, 2018. **19**: p. 160-166.
18. Körner, C., *Additive manufacturing of metallic components by selective electron beam melting — a review*. International Materials Reviews, 2016. **61**(5): p. 361-377.
19. Plotkowski, A., et al., *Evaluation of an Al-Ce alloy for laser additive manufacturing*. Acta Materialia, 2017. **126**: p. 507-519.
20. Körner, C., et al., *Microstructure and Mechanical Properties of CMSX-4 Single Crystals Prepared by Additive Manufacturing*. Metallurgical and Materials Transactions A, 2018. **49**(9): p. 3781-3792.
21. Raghavan, N., et al., *Localized melt-scan strategy for site specific control of grain size and primary dendrite arm spacing in electron beam additive manufacturing*. Acta Materialia, 2017. **140**: p. 375-387.
22. Lee, Y.S., et al., *Role of scan strategies on thermal gradient and solidification rate in electron beam powder bed fusion*. Additive Manufacturing, 2018. **22**: p. 516-527.

23. Barriobero-Vila, P., et al., *Peritectic titanium alloys for 3D printing*. Nat Commun, 2018. **9**(1): p. 3426.
24. Martin, J.H., et al., *3D printing of high-strength aluminium alloys*. Nature, 2017. **549**(7672): p. 365-369.
25. Croteau, J.R., et al., *Microstructure and mechanical properties of Al-Mg-Zr alloys processed by selective laser melting*. Acta Materialia, 2018. **153**: p. 35-44.
26. Simmons, J.W., *Overview: high-nitrogen alloying of stainless steels*. Materials Science and Engineering: A, 1996. **207**(2): p. 159-169.
27. Speidel, M.O., *Nitrogen Containing Austenitic Stainless Steels*. Materialwissenschaft und Werkstofftechnik, 2006. **37**(10): p. 875-880.
28. Li, H.-b., et al., *Mechanical Properties of Nickel Free High Nitrogen Austenitic Stainless Steels*. Journal of Iron and Steel Research, International, 2007. **14**(5): p. 330-334.
29. Yang, K. and Y. Ren, *Nickel-free austenitic stainless steels for medical applications*. Sci Technol Adv Mater, 2010. **11**(1): p. 014105.
30. Talha, M., C.K. Behera, and O.P. Sinha, *A review on nickel-free nitrogen containing austenitic stainless steels for biomedical applications*. Mater Sci Eng C Mater Biol Appl, 2013. **33**(7): p. 3563-75.
31. Schaaf, P., *Laser nitriding of metals*. Progress in Materials Science, 2002. **47**(1): p. 1-161.
32. Dong, W., et al., *Nitrogen desorption by high-nitrogen steel weld metal during CO2 laser welding*. Metallurgical and Materials Transactions B-Process Metallurgy and Materials Processing Science, 2005. **36**(5): p. 677-681.
33. Wang, X., et al., *Microstructure and yield strength of SLM-fabricated CM247LC Ni-Superalloy*. Acta Materialia, 2017. **128**: p. 87-95.
34. Dantzig, J.A. and M. Rappaz, *Solidification*. Materials, ed. M. Rappaz. Vol. 1. 2009, Lausanne, Switzerland: EPFL Press.
35. Tang, M., P.C. Pistorius, and J.L. Beuth, *Prediction of lack-of-fusion porosity for powder bed fusion*. Additive Manufacturing, 2017. **14**: p. 39-48.
36. Tang, M., et al., *Build Rate Optimization for Powder Bed Fusion*. Journal of Materials Engineering and Performance, 2018. **28**(2): p. 641-647.
37. Umeda, T. and T. Okane, *Solidification microstructures selection of Fe-Cr-Ni and Fe-Ni alloys*. Science and Technology of Advanced Materials, 2001. **2**(1): p. 231-240.
38. Umeda, T., T. Okane, and W. Kurz, *Phase selection during solidification of peritectic alloys*. Acta Materialia, 1996. **44**(10): p. 4209-4216.
39. Fukumoto, S. and W. Kurz, *Solidification Phase and Microstructure Selection Maps for Fe-Cr-Ni Alloys*. ISIJ International, 1999. **39**(12): p. 1270-1279.
40. Fu, J.W., Y.S. Yang, and J.J. Guo, *Microstructure selection of Fe-Cr-Ni alloy during directional solidification*. International Journal of Cast Metals Research, 2013. **23**(2): p. 119-123.
41. Scipioni Bertoli, U., et al., *In-situ characterization of laser-powder interaction and cooling rates through high-speed imaging of powder bed fusion additive manufacturing*. Materials & Design, 2017. **135**: p. 385-396.
42. Kenel, C. and C. Leinenbach, *Influence of cooling rate on microstructure formation during rapid solidification of binary TiAl alloys*. Journal of Alloys and Compounds, 2015. **637**: p. 242-247.